

Microstructure and hardening effect of pure tungsten and ZrO_2 strengthened tungsten under carbon ion irradiation at 700 ℃

Chun-Yang Luo(罗春阳), Bo Cui(崔博), Liu-Jie Xu(徐流杰), Le Zong(宗乐), Chuan Xu(徐川), En-Gang Fu(付恩刚), Xiao-Song Zhou(周晓松), Xing-Gui Long(龙兴贵), Shu-Ming Peng(彭述明), Shi-Zhong Wei(魏世忠), and Hua-Hai Shen(申华海)

Citation: Chin. Phys. B, 2022, 31 (**9**): 096102. DOI: 10.1088/1674-1056/ac6b25
Journal homepage: http://cpb.iphy.ac.cn; http://iopscience.iop.org/cpb

What follows is a list of articles you may be interested in

Structure, phase evolution and properties of Ta films deposited using hybrid high-power pulsed and DC magnetron co-sputtering

Min Huang(黄敏), Yan-Song Liu(刘艳松), Zhi-Bing He(何智兵), and Yong Yi(易勇)
Chin. Phys. B, 2022, 31 (**6**): 066101. DOI: 10.1088/1674-1056/ac43a9

Surface chemical disorder and lattice strain of GaN implanted by 3-MeV Fe^{10+} ions

Jun-Yuan Yang(杨浚源), Zong-Kai Feng(冯棕楷), Ling Jiang(蒋领), Jie Song(宋杰), Xiao-Xun He(何晓珣), Li-Ming Chen(陈黎明), Qing Liao(廖庆), Jiao Wang(王姣), and Bing-Sheng Li(李炳生)
Chin. Phys. B, 2022, 31 (**4**): 046103. DOI: 10.1088/1674-1056/ac373f

Temperature-dependent structure and magnetization of $YCrO_3$ compound

Qian Zhao(赵前), Ying-Hao Zhu(朱英浩), Si Wu(吴思), Jun-Chao Xia(夏俊超), Peng-Fei Zhou(周鹏飞), Kai-Tong Sun(孙楷橦), and Hai-Feng Li(李海峰)
Chin. Phys. B, 2022, 31 (**4**): 046101. DOI: 10.1088/1674-1056/ac2b23

Highly tunable plasmon-induced transparency with Dirac semimetal metamaterials

Chunzhen Fan(范春珍), Peiwen Ren(任佩雯), Yuanlin Jia(贾渊琳), Shuangmei Zhu(朱双美), and Junqiao Wang(王俊俏)
Chin. Phys. B, 2021, 30 (**9**): 096103. DOI: 10.1088/1674-1056/abf4bf

Formation of nano-twinned 3C-SiC grains in Fe-implanted 6H-SiC after 1500-℃ annealing

Zheng Han(韩铮), Xu Wang(王旭), Jiao Wang(王娇), Qing Liao(廖庆), and Bingsheng Li(李炳生)
Chin. Phys. B, 2021, 30 (**8**): 086107. DOI: 10.1088/1674-1056/abff43

Microstructure and hardening effect of pure tungsten and ZrO_2 strengthened tungsten under carbon ion irradiation at 700 °C

Chun-Yang Luo(罗春阳)[1,2,†], Bo Cui(崔博)[1,†], Liu-Jie Xu(徐流杰)[2,‡], Le Zong(宗乐)[2], Chuan Xu(徐川)[3], En-Gang Fu(付恩刚)[3], Xiao-Song Zhou(周晓松)[1], Xing-Gui Long(龙兴贵)[1], Shu-Ming Peng(彭述明)[1], Shi-Zhong Wei(魏世忠)[2], and Hua-Hai Shen(申华海)[1,2,§]

[1] *Institute of Nuclear Physics and Chemistry, China Academy of Engineering Physics, Mianyang* 621900, *China*
[2] *National & Local Joint Engineering Research Center for Abrasion Control and Molding of Metal Materials, Henan University of Science and Technology, Luoyang* 471003, *China*
[3] *Institute of Heavy Ion Research, Peking University, Beijing* 100871, *China*

(Received 20 February 2022; revised manuscript received 18 April 2022; accepted manuscript online 28 April 2022)

Microstructure evolution and hardening effect of pure tungsten and W–1.5%ZrO_2 alloy under carbon ion irradiation are investigated by using transmission electron microscopy and nano-indentation. Carbon ion irradiation is performed at 700 °C with irradiation damages ranging from 0.25 dpa to 2.0 dpa. The results show that the irradiation defect clusters are mainly in the form of dislocation loop. The size and density of dislocation loops increase with irradiation damages intensifying. The W–1.5%ZrO_2 alloy has a smaller dislocation loop size than that of pure tungsten. It is proposed that the phase boundaries have the ability to absorb and annihilate defects and the addition of ZrO_2 phase improves the sink strength for irradiation defects. It is confirmed that the W–1.5%ZrO_2 alloy shows a smaller change in hardness than the pure tungsten after being irradiated. From the above results, we conclude that the addition of ZrO_2 into tungsten can significantly reduce the accumulation of irradiated defects and improve the irradiation resistance behaviors of the tungsten materials.

Keywords: W–ZrO_2 alloy, carbon ion irradiation, microstructure, surface hardness

PACS: 61.82.Bg, 61.80.Lj, 61.80.–x, 62.20.Qp **DOI:** 10.1088/1674-1056/ac6b25

1. Introduction

The development of controlled thermonuclear fusion energy plays an important role in the development of nuclear energy. Thermonuclear fusion reactor materials are one of the major challenges that prevent fusion reactors from moving toward engineering applications and commercialization.[1–3] In particular, the plasma-facing materials (PFMs) in fusion reactors work in a very severe environment. Energy conversion takes place during the fusion reactions of D and T. The PFMs are subjected to complex multi-field coupling effects, including the bombadment of plasma particles (D^+, T^+, and He^+ with 3.5 MeV) and fast neutrons (14.1 MeV), and high thermal loads ($\sim$ 20 MW/m^2). In general, the PFMs should have good thermodynamic properties (high melting point, good thermal conductivity, and high thermal shock resistance), low sputtering yield (low quantity of impurities from sputtering and irradiation-enhanced sublimation), low gas absorption to the plasma, and low radioactivity.[4,5] Tungsten (W) is considered to be one of the most promising PFMs due to its high melting point, good thermal conductivity, and high sputtering threshold.[6,7] However, the tungsten serving as a plasma-oriented material still faces great challenges.

In the nuclear fusion reactor, the properties of PFM are critical to the safe and efficient operation of the entire reactor. The presence of fast neutrons with high power makes PFMs exposed to high levels of irradiation damage. Fast neutrons collide with atoms to cascade collisions, creating a large number of defects within the material and preventing dislocations from moving, thus leading its hardness to increase and the plastic toughness of the material to decrease.[8] At the same time, a large number of defects act as traps to elevate the plasma retention.[9] Fast neutron irradiation transmutes tungsten into other elements such as rhenium and osmium, and the transmutation products cause irradiation deposition, irradiation hardening, and irradiation embrittlement.[10,11] The ductile–brittle transition temperature of tungsten increases after being irradiated by neutrons, and even a small damage of neutron irradiation can create severe irradiation hardening of the material. It is crucial to improve the toughness of tungsten and reduce its irradiation hardening effect.

Researchers have been continuously improving the comprehensive properties of tungsten through composition design and preparation processes. The W alloys produced by spark plasma sintering (SPS) exhibit excellent tensile properties,[12] but currently the large bulk tungsten is mainly produced by embryo making, sintering, and thermomechanical treatment

[†]These authors made equal contributions to this work.
[‡]Corresponding author. E-mail: wmxlj@126.com
[§]Corresponding author. E-mail: huahaishen@caep.cn

© 2022 Chinese Physical Society and IOP Publishing Ltd

(hot rolling, swaging). Dispersion strengthening (oxide dispersion strengthening, carbon dispersion strengthening, *etc.*) method can inhibit grain growth, reduce grain size, improve the grain boundary strength and fracture toughness of the material, and reduce the ductile–brittle transition temperature. Fiber reinforcement can largely alleviate the brittleness of tungsten and improve the fracture toughness of W through mechanisms such as fracture, pull-out, and bridging of W fibers.[13] Solid solution strengthening (Ta, Nb, Re, *etc.*) improves the strength of W by improving the grain boundary strength, and the addition of rhenium can inhibit the formation of cavities during neutron irradiation.[10] Combined with the current research status, introducing particles, such as ZrC, TiC, La_2O_3, and Y_2O_3, into the tungsten matrix can enhance their mechanical properties. The ZrO_2 particle-reinforced tungsten alloy is prepared by azeotropic distillation, powder metallurgy, and thermo-mechanical processing in combination with the production process of tungsten. The distribution and content of ZrO_2 are adjusted to refine the grain size and improve the strength and toughness of the tungsten.[14] However, the effects of strengthened precipitates on the irradiation damages of tungsten alloys have been less studied. In particular, the interaction mechanism between the irradiation induced defects and the strengthening phase under high-temperature irradiation conditions is not clear. The changes in the mechanical properties of the material after irradiation need further investigating.

In this work, we study the microstructure evolution and mechanical properties of W and W–1.5%ZrO_2 alloy under carbon ion irradiation. The irradiation temperature is set to be at 700 °C, and the carbon ion energy is 3 MeV, and the irradiation doses are 1.7×10^{15} ions/cm^2, 3.4×10^{15} ions/cm^2, 6.8×10^{15} ions/cm^2, and 1.4×10^{16} ions/cm^2, respectively. Transmission electron microscopy (TEM) is used to characterize the irradiation defects and to explore the irradiation mechanism of the dislocation loop distribution of second phase ZrO_2 and the phase boundaries. The changes of surface hardness after ion irradiation are analyzed by using the nano-indentation. Moreover, the effects of second-phase ZrO_2 on irradiation defects and mechanical properties are systemically investigated and discussed.

2. Experiment

The materials under study were W and W–1.5wt% ZrO_2 alloy. The two materials were prepared by azeotropic distillation, powder metallurgy, and high-temperature spin-forging methods. The grain size of the material was reduced by thermomechanical treatment.[14] The ion irradiated samples were 2 mm × 2 mm × 1 mm in size. The pre-irradiated surfaces were ground by using SiC sandpaper and polished with polishing solution to ensure that there were no obvious scratches on the surfaces of the samples. The samples were annealed at 1400 °C for 1 h to remove the stress concentration generated in the machining and grinding process.

Heavy ion irradiation was carried out at the Institute of Heavy Ion Physics, Peking University. The samples were irradiated by 3-MeV carbon ions at 700 °C with four preset irradiation doses: 1.7×10^{15} ions/cm^2, 3.4×10^{15} ions/cm^2, 6.8×10^{15} ions/cm^2, and 1.4×10^{16} ions/cm^2, respectively.

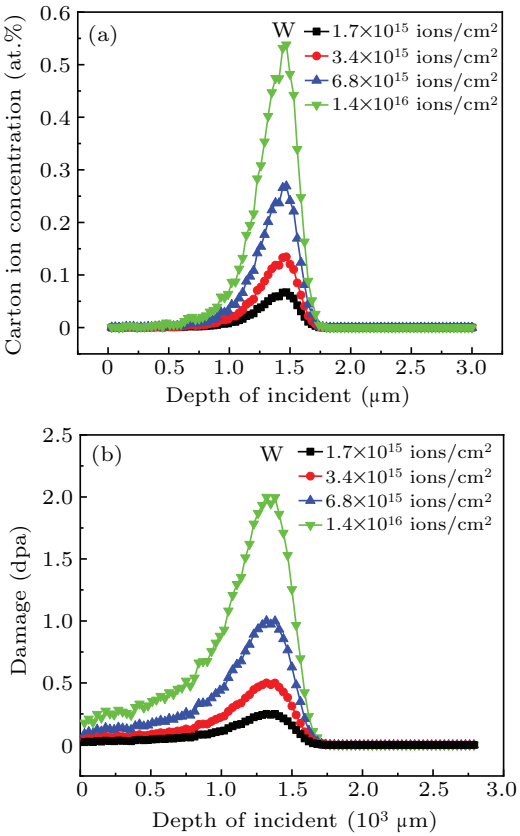


Fig. 1. Variations of (a) carbon ion concentration and (b) irradiation damage with depth of incidence for different ion concentrations.

The displacement energy of W atoms was 90 eV, and the Stopping and Range of Ions in Matter (SRIM) program was used to simulate the process of carbon ions incident on the W target and to determine the distribution of damage and incident carbon ion concentration in the W target along the depth of incidence. In the SRIM program adopted is the detailed calculation with full damage cascades mode to simulate 10^4 carbon ions continuously bombarding the target. The distribution of irradiation damage and the distribution of carbon ion concentration with depth were plotted according to the SRIM simulation results, and their results are shown in Fig. 1. The four doses that can create damage were 0.25 dpa, 0.5 dpa, 1.0 dpa, and 2.0 dpa. From Fig. 1, it can be seen that the distribution of carbon ion concentration and the distribution of irradiation damage are normally distributed, and the carbon ion concen-

tration and irradiation damage increase with the depth of incidence, and then decrease rapidly after reaching a maximum value. The maximum concentration value appears at 1370 nm. The distributions of irradiation damage were similar to each other at different total irradiation damages, and all reached their corresponding maximum damage values at 1200 nm.

The TEM specimens were prepared by using the focused ion beam (FIB). For the samples prepared by FIB, the defect distribution at different locations along the incident direction can be observed. The irradiated samples were studied by an FEI Tecnai G2 F30 TEM. The contrast of the dislocation loop image is more pronounced when observed under two-beam or weak-beam conditions. In this experiment, the density and diameter of dislocation loops of the different irradiated samples were characterized by using the two-beam bright-field TEM condition with a $\boldsymbol{g}$ vector of (110). The five regions were observed and counted in cross-sectional TEM samples at the same depth to improve statistical accuracy. The size and number of dislocation loops were determined by treating them as solid granular objects, and solid particles were counted by Image J software.

The hardening effects of irradiated samples were measured at room temperature by using a Keysight Nano-Indenter G200. A continuous stiffness measurement method with a constant loading rate of 0.05 nm/s was used for all experiments. To minimize experimental errors, at least 20 test points were performed for each specimen and the average of the experimental results was taken. The hardness changes with depth, and the deeper the indentation depth, the closer to the substrate hardness value the hardness value is, and this phenomenon is called the substrate effect.[15] In this experiment, the indentation depth of the indenter was set to be 1500 nm. As is well known, simply reporting and analyzing the measured nano-hardness at a single depth is not acceptable. The Nix–Gao method[16–18] was used to estimate the bulk equivalent hardness in this study.

3. Results and discussion

Figure 2 shows the corresponding microstructure of W and microstructure of W–1.5%ZrO_2 alloy. The average grain size of W is $\sim$ 35 μm, the average grain size of the W–1.5%ZrO_2 alloy is $\sim$ 12 μm, and the average grain size of the second phase particles ZrO_2 is 0.5 μm and its number density is about 9.55×10^{16} m^{-3}. The ZrO_2 particles is distributed along the grain boundaries.

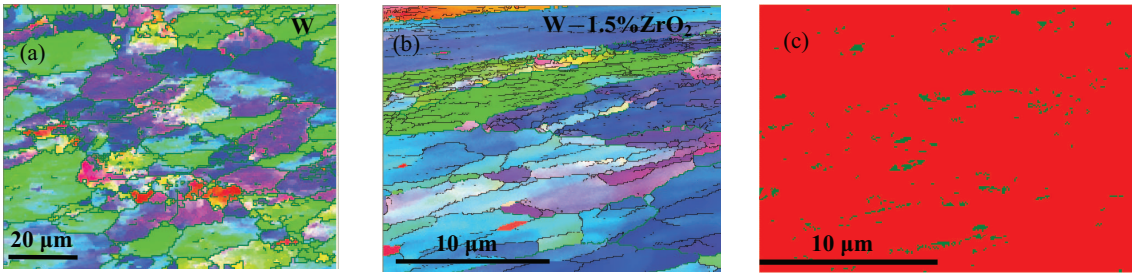


Fig. 2. EBSD Inverse pole figure (IPF) map of (a) W, (b) W–1.5%ZrO_2, and (c) phase distribution diagram, with red area representing W phase and green area denoting ZrO_2 phase.

Figure 3 shows the low magnification TEM image of the W–ZrO_2 alloy. It can be seen from the figure that theTEM sample consists of three main parts: Pt protective layer, white particles, and W matrix, as shown in Fig. 3(a). It can be observed that the size of the white particle is about 700 nm, and there are no obvious pores at the interface between the white particles and the matrix. To further confirm their composition, the EDS analysis of the regions e and f in Fig. 3(a) is carried out. The matrix part c consists mainly of for W elements, and the composition of particle d consists of Zr and O for the ZrO_2 phase. Diffraction spots analysis is performed in the regions c and d in Fig. 3(a). The diffraction spots of the matrix in Fig. 3(c) show that the matrix is a bodycentered cubic structure of W with a zone axis of [001]. Figure 3(d) shows the diffraction spots of the white particles, indicating that the white particle is the facecentered cubic zirconia particle with the zone axis [011]. Zirconia particles exposed to the sample surface that can directly withstand ion irradiation are used to analyze the effect of ion irradiation on zirconia. In the preparation of TEM samples of W–ZrO_2 alloy, the region containing zirconia particles is purposely selected for preparation.

Figure 4 shows typical damaged microstructure of W and that of W–1.5% ZrO_2 alloys at different doses. All micrographs are taken under two-beam kinematical bright-field condition by using $\boldsymbol{g} = 110$. A large number of dislocation loops are observed in samples. It could be seen from the figure that the number of dislocation rings and the diameter in the sample increase with irradiation dose increasing. However, large dislocation loops and small dislocation loops are interspersed in the samples, and some of the dislocation loops are entangled to form dislocation networks, which is not conducive to the accurate counting of the number and diameter of dislocation rings.

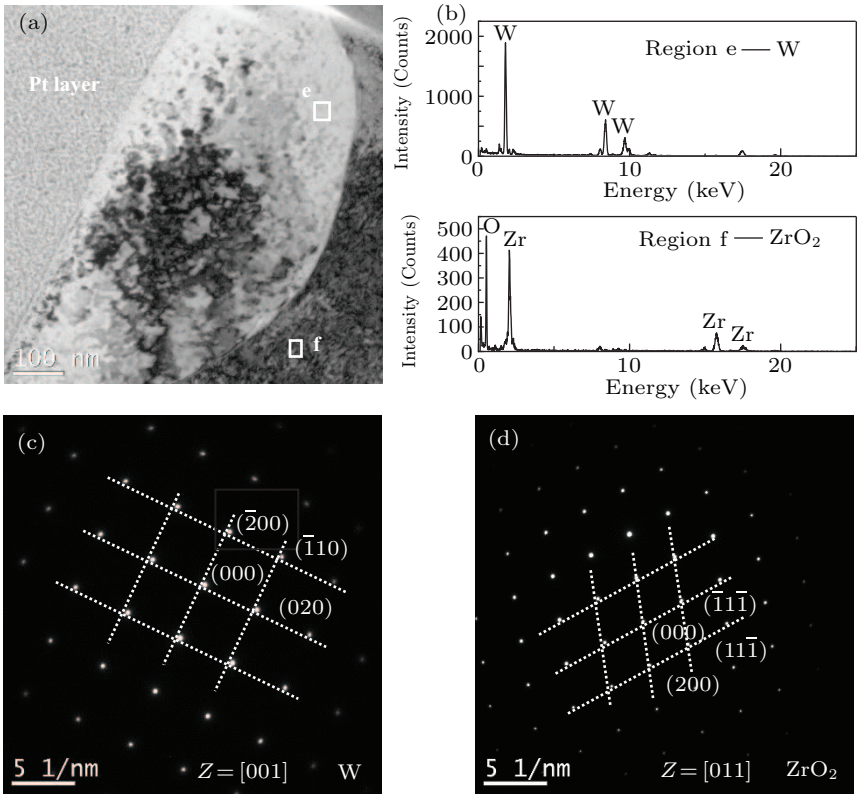


Fig. 3. (a) Low magnification TEM image, (b) EDS analysis of regions e and f in panel (a), (c) diffraction spots in region e in panel (a), and (d) diffraction spots in region f in panel (a), of W–ZrO_2 alloy.

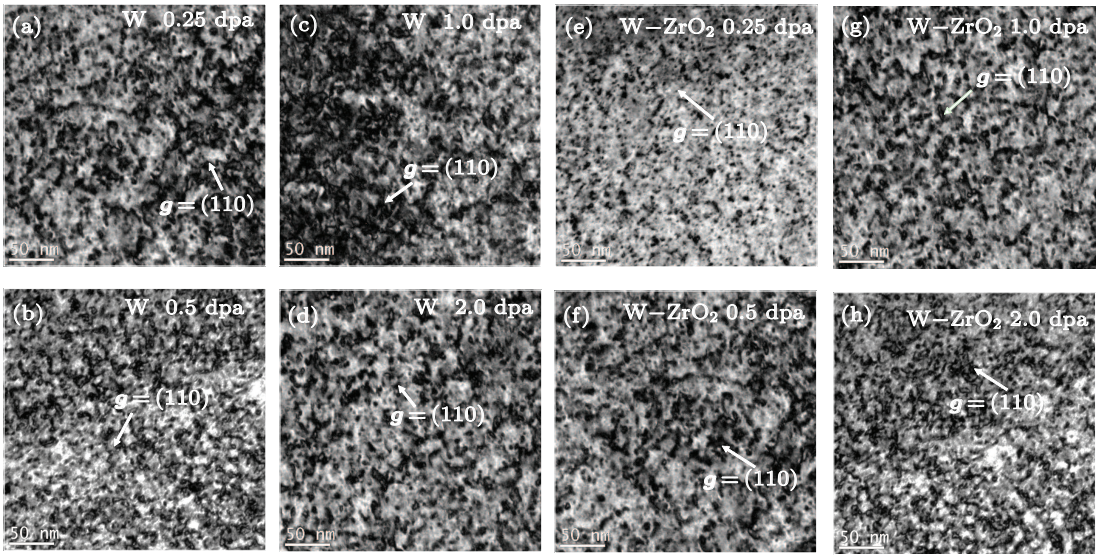


Fig. 4. Micrographs of dislocation loops for tungsten and tungsten alloys, taken under two-beam kinematical bright-field condition using $\boldsymbol{g} = 110$ (indicated by white arrows).

As is well known, there are generally two types of dislocation loops with a Burgers vectors of $\langle 100 \rangle$ and $1/2\langle 111 \rangle$ in body-centered cubic materials. The types of loops are determined based on the observed extinction conditions for the different diffraction vectors. However, the number of dislocation loops is so large that it is impossible to count all the dislocation loops under multiple vectors, and the dislocation loop vectors can be observed and counted by two different $\boldsymbol{g}$ vectors. Figure 5 shows the images obtained under different extinction conditions, the red area in the figure represents the same location, but no dislocation loop is found in the red circle in Fig. 5(b). These TEM images are taken under two-beam conditions near [100] axis zone, in which Fig. 5(a) is used by $\boldsymbol{g}$ vector $\langle 110 \rangle$, while figure 5(b) is used by $\boldsymbol{g}$ vector $\langle 002 \rangle$. The observation of the thickness stripes reveals that the thickness of the area observed and analyzed is relatively uniform, which facilitates the calculation of the volume of the analyzed area (approximated as a rectangle). The total density of dislocation loops in the region is calculated according to the ratio of the occurrence of two types of dislocation loops under different

extinction conditions in the body-centered cubic material as shown in the following equation:[19]

$$\rho = \frac{1}{3}\rho_{g=\langle 200\rangle} + \frac{4}{3}\rho_{g=\langle 110\rangle}. \quad (1)$$

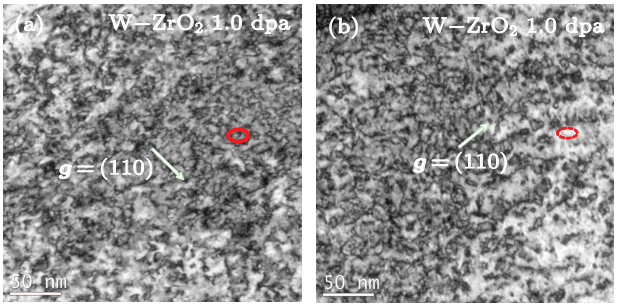


Fig. 5. Bright-field TEM images under two beams from [100] zone axis, showing loops in W–1.5%ZrO_2 with 4.0-dpa irradiation damage, with (a) $\boldsymbol{g}$ vector of $\langle 110\rangle$ and (b) with $\boldsymbol{g}$ vector of $\langle 002\rangle$.

Figure 6(a) gives the curves of volume number density of dislocation loops in W and W–1.5%ZrO_2 alloy *versus* dose. The bulk density of dislocation loops increases with irradiation damage increasing. At low irradiation doses (< 1.0 dpa), the dislocation loop density increases significantly. However, the overall trend is weak, especially after the irradiation damage has reached 1.0 dpa, the dislocation loop density tends to flatten out. Under the same irradiation conditions, the dislocation loop density in W is higher than that in W–1.5%ZrO_2. When the irradiation damage is 1.0 dpa, the dislocation loop density in pure tungsten is 1.7×10^{23} m^{-3} and in W–1.5%ZrO_2 alloy is 1.5×10^{23} m^{-3}. In Fig. 4, it can be found that the phenomenon of agglomeration and merging of dislocation loops occurs in W. Meanwhile, the defects in the grains are more likely to grow and aggregate under 700-°C irradiation. The dislocation loop density of pure tungsten remains essentially constant when the irradiation damage reaches 2.0 dpa, considering that the dislocation loop density generated by irradiation maybe reaches saturation at 1.0 dpa. However, the dislocation loop density in W–1.5%ZrO_2 still maintains a slow increasing rate. Owing to the limited variation of irradiation damages involved in the experiments, it is not yet possible to determine whether the dislocation loop density in the W–1.5%ZrO_2 alloy reaches saturation.

Quantitative analysis of dislocation loop size in W and in W–1.5%ZrO_2 alloys are performed. The average diameter of dislocation loops is then calculated by the near-circle method as shown in Fig. 6(b). As the irradiation damage increases, the diameter of the dislocation loop becomes larger, and the increasing trend of the diameter gradually becomes slower. When the irradiation damage is 0.25 dpa, the dislocation loop diameter is 2.9 nm in W and 2.6 nm in W–1.5%ZrO_2 alloy. When the irradiation damage increases to 1.0 dpa, the dislocation loop diameterincreases to 3.7 nm in W and 3.3 nm in W–1.5%ZrO_2 alloy. The dislocation loop diameter in W remains stable, while the dislocation loop diameter in W–1.5%ZrO_2 alloy is still growing. Combining the changes of dislocation loop density and diameter in W–1.5%ZrO_2 alloy, it can be assumed that the dislocation loop in W–1.5%ZrO_2 alloy does not yet reach saturation.

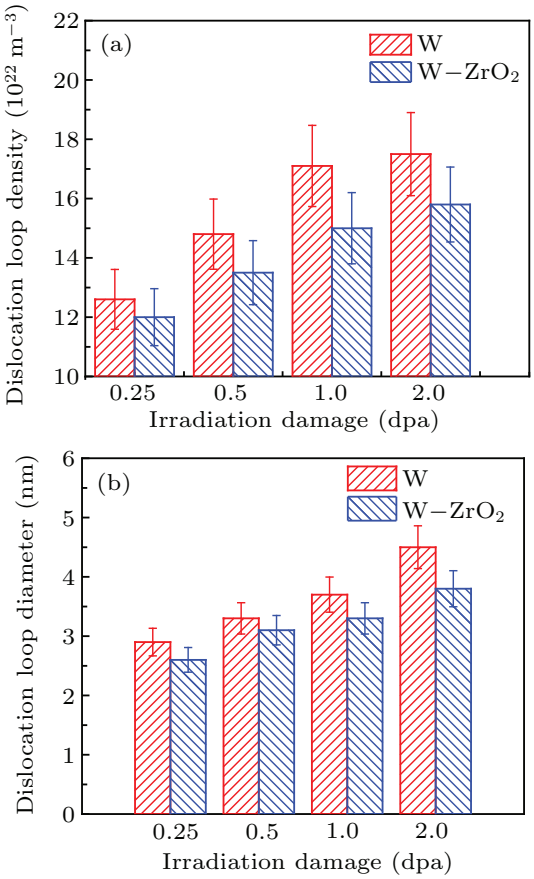


Fig. 6. Curves of loop density in pure W and W–1.5ZrO_2 *versus* irradiation damage for (a) total dislocation loop density and (b) dislocation loop diameter.

In the low damage range (0.25 dpa–1.0 dpa), it is evident that the dislocation loop density and diameter increase with irradiation damage increasing. However, with the further increase of irradiation damage, the variation of dislocation loop density and diameter tend to stabilize. During the irradiation, the tungsten atoms undergo cascade collisions to continuously generate interstitial atoms and vacancies. On the one hand, the continuously generated new defects can nucleate, forming new dislocation loops, and on the other hand, they can accumulate on the existing dislocation loops, resulting in dislocation loops with a larger size. When the irradiation damage is low, the nucleation rate of point defects is higher than the annihilation rate of point defects. The nucleated point defect clusters absorb the newly generated point defects around them. The cluster grows when the cluster has the same properties as the absorbed point defects.

The grain boundary and the phase boundary are usually considered to have good absorption of interstitial atoms and vacancies. The sink strength of the grain boundary and the

ZrO_2 phase boundary can be calculated from the following equations:[20,21]

$$S_g = \frac{15}{h^2}, \tag{2}$$

$$S_p = 4\pi N (0.3A)^{1/2}, \tag{3}$$

where S_p is the sink strength contributed from oxides; N is the number density of ZrO_2; A is the surface area of ZrO_2, and $A = 4\pi r^2$; r is the average radius of ZrO_2; S_g is the sink strength contributed from grain boundaries; h is the average grain size. Based on the microstructure statistics of W and the W–1.5%ZrO_2 alloy, the sink strength S_{g1} of grain boundaries in pure tungsten is 1.22×10^{10} m^{-3} from Eq. (2), and that of S_{g2} in W–1.5%ZrO_2 alloy is 1.04×10^{11} m^{-3}. The sink strength of grain boundaries in W–1.5%ZrO_2 alloy is 8.5 times higher than that of W. The addition of ZrO_2 limits the grain growth of the tungsten, offering higher density grain boundaries that can absorb and annihilate more defects. The sink strength of the phase boundary is calculated to be 1.16×10^{12} m^{-3}, which is 10 times the value of the grain boundary strength. On the whole, figures and calculations show that the phase boundaries of ZrO_2 and tungsten have higher absorbing strength than the grain boundaries. Therefore, it can be assumed that the phase boundary plays a dominant role in annihilating the irradiation.

Figure 7 shows the tungsten grain boundaries and the phase boundaries between tungsten and ZrO_2 phase in W and W–1.5%ZrO_2 alloy. Observing the dislocation distribution near the grain boundaries, we can see that the density of dislocation loop near the grain boundaries decreases as shown in Figs. 7(a) and 7(b). This is called denuded zone. The existing of free loop zone indicates that the boundaries can significantly absorb the defects in the vicinity. The phase boundary between W and ZrO_2 similarly exhibits an absorbing effect on irradiation defects as shown in Fig. 7(c). A distinct dislocation-denuded zones appear at the phase boundary located on the side of the W grain, which is distributed along the phase boundary with a width of 20 nm–30 nm (marked by red lines in the figure). The density of dislocation loops near the denuded zonesignificantly decreases. These phenomena indicate that the phase boundary can effectively absorb and annihilate the defects generated after irradiation and outperforms the effect of the grain boundary. And this result is consistent with the previously calculated result of the sink strength of the interface, where the phase boundaries of W and of ZrO_2 have the effect of sinking-irradiated dislocations far beyond the tungsten grain boundary. In summary, the addition of ZrO_2 particles can hinder the tungsten grains from growing, increase the density of grain boundaries, and provide the phase boundary. The absorption and annihilation of irradiation defects are significantly improved in the W–1.5%ZrO_2 alloy, resulting in enhanced irradiation resistance of the tungsten alloy.

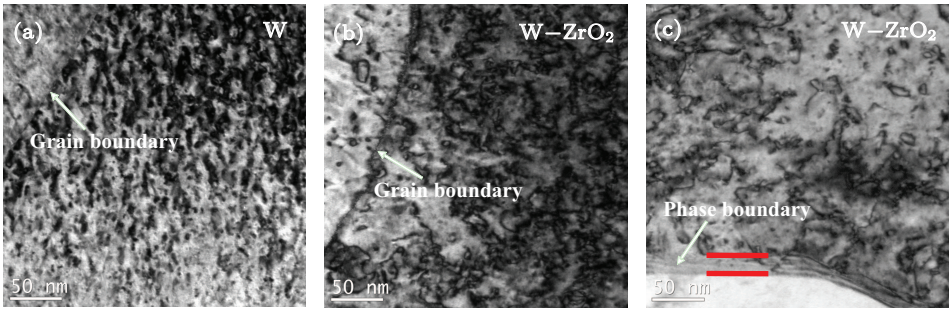


Fig. 7. (a) Grain boundaries in pure tungsten and (b) grain boundaries in W–1.5ZrO_2 alloy, and (c) phase boundaries in W–1.5ZrO_2 alloy.

The variation of surface hardness of ion irradiated samples is measured by using the nano-indentation technique. Figures 8(a) and 8(b) show the curves of hardness variation of the two tested materials versus depth after irradiation. As a whole, the two materials show obvious irradiation hardening phenomenon, and the irradiation hardening phenomenon becomes more and more obvious with the increase of irradiation damage. The hardness value gradually decreases with depth increasing. However, many studies have pointed out that nano-indentation does not provide a true hardness measurement at each depth.[16] Takayama *et al.*[22] proposed the Nix–Gao[17] model (Eq. (4)) to evaluate the equivalent hardness, considering the indentation size effect[18] and the soft substrate effect[23] on hardness,

$$H = H_0 \sqrt{1 + \frac{h_c}{h}}, \tag{4}$$

where H_0 is the hardness at infinite depth, h_c is the characteristic length that depends on the material and the shape of the indenter tip, H is the hardness value when the depth is h. A dotted line plot of H^2 *versus* $1/h$ according to the Nix–Gao model is shown in Figs. 8(c) and 8(d), separately. The non-irradiated samples have a good linearity above ~ 75 nm in indentation depth. The irradiated samples, on the other hand, exhibit linearity with the turning point roughly between 250 nm and 375 nm in indentation depth. This is mainly due to the fact that irradiation hardening is present on the sample sur-

face, while the hardness inside the sample does not change significantly, and the hardness of softer substrate decreases as the indentation depth increases. The turning point of the hardness change here is about 1/6 of the depth of the damaged layer, which is consistent with previous studies.[24] The hardness of the sample is expressed by using H_0 in a range of 75 nm–375 nm for non-irradiated and irradiated samples. The statistical results are shown in Table 1. When the irradiation damage is 0.25 dpa, the hardness value of W–1.5%ZrO_2 alloy is 6.4 GPa, which is lower than that of W at 6.6 GPa, which is consistent with the nature of its matrix.[14] The addition of zirconia particles refines the grains and hinders the dislocation from moving, which increases the hardness of the tungsten alloy. However, with the increase of irradiation damage, the surface hardness of W rapidly increases, and when the irradiation damage reaches 2.0 dpa, its hardness value arrives at 9.3 GPa, which increases by 41%. At this time, the hardness value of W–1.5%ZrO_2 alloy changes slowly and reaches 8.5 GPa when the irradiation damage rises up to 2.0 dpa, which is 32% higher than the initial damage. The results indicate that the irradiation hardening effect of the W–1.5%ZrO_2 alloy is lower, suggesting that the addition of zirconia particles is beneficial to improving the resistance to irradiation hardening. Combined with the previous analysis of irradiation defects in both materials, this result is not so difficult to understand. The coarse grains and low grain boundary density in W can limit the sink effect on defects at grain boundaries, resulting in a large accumulation of irradiation defects within the W grains, which severely impedes the movement of dislocations and increases the surface hardness. However, the addition of ZrO_2 particles refines the W grains and increases to a larger number of grain boundaries, which improves the defect sinking efficiency. Otherwise, the phase boundaries introduced by the ZrO_2 particles have a sink strength far beyond the grain boundaries, reducing the accumulation of defects within the W grains. Therefore, the W–1.5%ZrO_2 alloy has the potential to be used as a plasma-facing material in fusion reactor.

Table 1. Summary of nano-hardness for W and W–1.5%ZrO_2 alloy.

Materials	H (GPa)			
	Irradiation 700 °C			
	0.25 dpa	0.5 dpa	1.0 dpa	2.0 dpa
W	6.6	7.4	8.5	9.3
W–1.5%ZrO_2	6.4	7.0	7.8	8.5

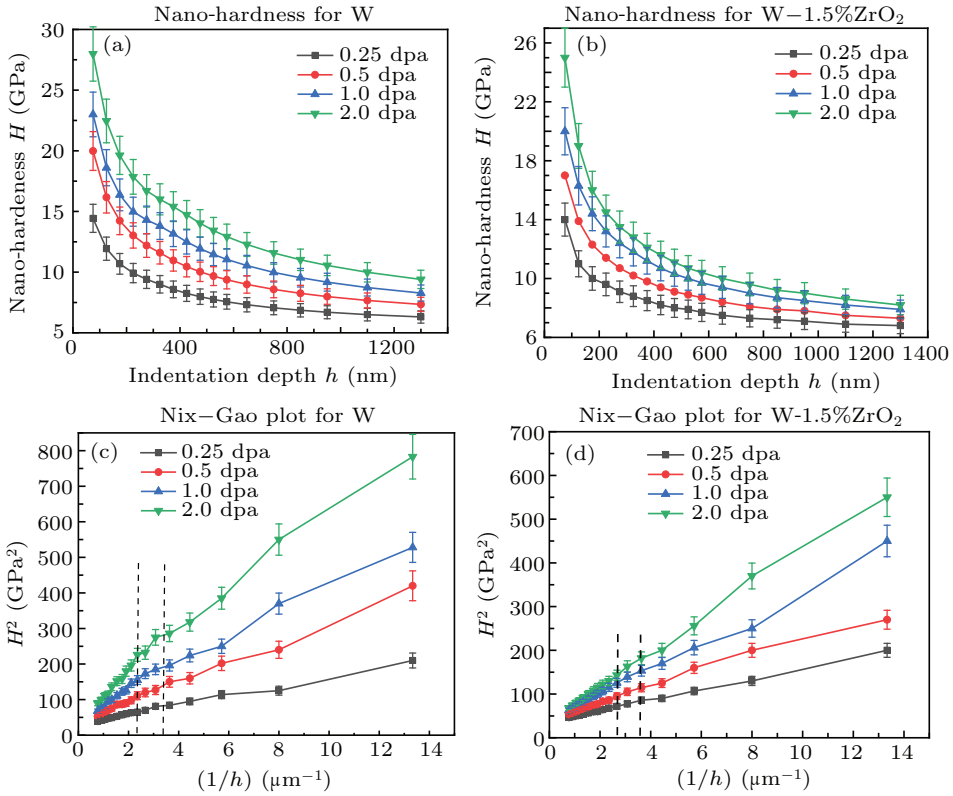


Fig. 8. Irradiation hardening effect statistics of irradiated samples, showing [(a) and (b)] corresponding hardness–displacement curves, and [(c) and (d)] experimental hardness values at the depth of 400 nm–1000 nm from surface.

4. Conclusions

W and W–1.5%ZrO_2 alloy are irradiated with carbon ions at 3.0 MeV and 700 °C with irradiation damages ranging from 0.25 dpa to 2.0 dpa. The microstructural evolutions and surface hardness values of the two materials after being irradiated are investigated and compared to explore the role of the second phase ZrO_2. The main results of this study are as follows.

(i) The dislocation loop density and diameter increase with the increase of irradiation damage, but show signs of stabilization. The dislocation size decreases significantly with the addition of ZrO_2 increasing.

(ii) The grain boundary and phase boundary can absorb and annihilate the defects. The addition of ZrO_2 particles increases the grain boundary density of the tungsten alloy and improves the ability of the grain boundaries to sink defects. The phase boundary of W–1.5%ZrO_2 possesses a sink strength that is much higher than that of the W grain boundary, reaching 1.16×10^{12} m^{-3}.

(iii) More obvious loop aggregations are created in W at 700-°C irradiation temperature. The dislocation loop diameters and densities in W are larger than those of the W–1.5%ZrO_2 alloy.

(iv) The irradiation hardening effect of W–1.5%ZrO_2 is lower than that of W. The addition of ZrO_2-reinforced phase increases the density of grain boundaries in W–1.5% ZrO_2 and provides the W–ZrO_2 phase boundaries, which improves the sink effect of the interface on defects, absorbs and annihilates the point defects, reduces the formation of dislocation loops, and the accumulation of irradiation defects, resulting in weaker irradiation hardening.

Acknowledgements

Project supported by the President's Foundation of the China Academy of Engineering Physics (Grant No. YZJJLX2018003), the National Natural Science Foundation of China (Grant Nos. U2004180 and 12105261), and the Program for Changjiang Scholars and Innovative Research Team in Universities, China (Grant No. IRT1234).

References

[1] Ongena J and Ogawa Y C 2016 *Energy Policy* **96** 700
[2] Tanabe T, Wada M, Ohgo T, Philipps V and Schweer B 2000 *J. Nucl. Mater.* **283** 1128
[3] Aymar R 2002 *Fusion Engineering and Design* **61** 5
[4] Matera R and Federici G 1996 *J. Nucl. Mater.* **233–237** 17
[5] Pitts R A, Carpentier S, Escourbiac F, Hirai T, Komarov V, Kukushkin A S, Lisgo S, Loarte A, Merola M and Mitteau R 2011 *J. Nucl. Mater.* **415** S957
[6] Maisonnier D, Cook L, Pierre S, Lorenzo B, Di P L, Luciano G, Prachai N and Aldo P 2006 *Fusion Engineering & Design* **81** 1123
[7] Rieth M, Armstrong D, Dafferner B, Heger S, Hoffmann A, Hoffmann M D, Jantsch U, Kübel C, Edeltraud M M, Jens R, Magnus R, Torsten S, Verena W and Horst Z 2010 *Adv. Sci. Technol.* **73** 11
[8] Wu Y C 2019 *Acta Metallurgica Sinica* **55** 939
[9] Shimada M, Hatano Y, Calderoni P, Oda T, Oya Y, Sokolov M, Zhang K, Cao G, Kolasinski R and Sharpe J P 2011 *J. Nucl. Mater.* **415** S667
[10] Fukuda M, Yabuuchi K, Nogami S, Hasegawa A and Tanaka T 2014 *J. Nucl. Mater.* **455** 460
[11] Tanno T, Hasegawa A, He J C, Fujiwara M, Nogami S, Satou M, Shishido T and Abe K 2007 *Mater. Trans.* **48** 2399
[12] Rieth M and Dudarev S 2013 *J. Nucl. Mater.* **442** S172
[13] Riesch J, Han Y, Almanstotter J, Coenen J W, Hoschen T, Jasper B, Zhao P, Linsmeier C and Neu R 2013 *Phys. Scr.* **2013** 014006
[14] Li Z, Xu L J, Wei S Z, Chen C and Xiao F N 2018 *J. Alloys Compd.* **769** 694
[15] Das S, Yu H, Mizohata K, Tarleton E and Hofmann F 2019 **135**
[16] Huang H F, Gao J, Radiguet B, Liu R D, Li J J, Lei G H, Huang Q, Liu M and Xie R B 2018 *J. Nucl. Mater.* **499** 431
[17] Nix W D and Gao H 1998 *J. Mech. Phys. Solids* **46** 411
[18] Pharr G M, Herbert E G and Gao Y F 2010 *Annu. Rev. Mater. Res.* **40** 271
[19] Guo L P, Luo F F and Yu Y X 2017 *Dislocation Loops in Irradiated Nuclear Materials* (Beijing: National Defense Industry Press) p. 114
[20] Lu C Y, Lu Z, Wang X, Xie R, Li Z Y, Higgins M, Liu C M, Gao F and Wang L M 2017 *Sci. Rep.* **7** 40343
[21] Sun C, Bufford D, Chen Y, Kirk M A, Wang Y Q, Li M, Wang H, Maloy S A and Zhang X 2014 *Sci. Rep.* **4** 3737
[22] Takayama Y, Kasada R, Sakamoto Y, Yabuuchi K and Tanigawa H 2013 *J. Nucl. Mater.* **S442** 23
[23] Kasada R, Takayama Y, Yabuuchi K and Kimura A 2011 *Fusion Engineering & Design* **86** 2658
[24] Huang H F, Li J J, Li D H, Liu R D, Lei G H, Huang Q and Yan L 2014 *J. Nucl. Mater.* **454** 168